Early Stages of Fatigue Crack Initiation in Relation With Twin Boundaries in Polycrystalline Ni-Based Superalloy AD730™

JULIEN PROUTEAU, PATRICK VILLECHAISE, LOIC SIGNOR, and JONATHAN CORMIER

Fatigue crack initiation in polycrystalline γ/γ' Ni-based superalloys depends on many factors such as loading conditions, temperature, environment, and microstructure. From room to intermediate temperatures, cracks are frequently related to twin boundaries in the coarse grains. The local conditions favoring cracks along the twin boundaries are analyzed in this paper considering the cast and wrought AD730™ alloy with a bimodal grain structure. Rupture and interrupted fatigue tests have been performed at room temperature under total strain control. Surface observations at the beginning of the fatigue life allowed a statistical analysis of cracks which occur mainly along the twin boundaries. The plasticity and local slip configurations have been discussed with the support of fine observations of cracks and plasticity traces. The orientation of the slip with respect to the free surface varies considerably with the loading amplitude and seems to impact the crack initiation mechanisms.

I. INTRODUCTION

IN aircraft engines, polycrystalline cast and wrought Ni-based superalloy turbine disks are critical parts subjected to a complex fluctuating stress state and a wide temperature range [20 °C to 700 °C]. The control of the microstructure through specific heat treatment steps is crucial to achieve the required mechanical properties, especially creep and fatigue ones. Among all the microstructural characteristics, the control of the grain size is the key element for the fatigue design of the bore region of turbine rotors which experience higher stresses and lower temperatures.[1] Even if the grain size is industrially carefully controlled, a variability may exist at the scale of a component. It is thus important to study the configurations that can lead to the initiation of a crack. At room and intermediate temperatures, fatigue crack initiation in Ni-based superalloys is often related to the accumulation of plastic deformation in coarse grains along the twin boundaries (TBs).[2–5] At higher temperatures, the initiation modes are controlled by the level of stress with surface initiation by oxidation in LCF[6] and competition between TBs and non-metallic inclusions at lower stress amplitudes in HCF.[7]

In alloys free of large internal defects and at moderate temperatures, the fatal cracks initiate preferentially on the largest grains, which results in large crystallographic facets on the fracture surface,[2,8] because of the easy slip transmission, which promotes highly localized slip bands over long slip lengths. Clusters of grains with low misorientation were also reported to be weak points referred to as "supergrain."[9] This phenomenon has been quantified by DIC–EBSD analysis in Reference 10.

Classically, fatigue crack initiation at the surface of polycrystalline metals and alloys is often associated with slip band intrusions/extrusions under fully reversed loading conditions.[11] Numerous studies have been conducted on fatigue crack initiation in slip bands in pure metals, highlighting the impact of the characteristics of slip bands and the associated surface topography.[12–14] In Ni-based superalloys, the plastic deformation is more localized than in pure metals, and results in thin slip bands with high plastic strain accumulation.[6,15] The use of atomic force microscopy

JULIEN PROUTEAU, PATRICK VILLECHAISE, LOIC SIGNOR, and JONATHAN CORMIER are with the Physics and Mechanics of Materials Department, Institut Pprime, CNRS - ENSMA - Université de Poitiers, UPR CNRS 3346, ISAE-ENSMA - Téléport 2, 1 avenue Clément Ader, BP 40109, 86961 Futuroscope Chasseneuil Cedex, France. Contact e-mail: julien.prouteau@ensma.fr Manuscript submitted September 6, 2022; accepted November 21, 2022.
Article published online December 10, 2022

has made it possible in some cases to correlate crack initiation to the height of the slip band extrusions[16] or to a critical level of local irreversible plastic strain accumulated on the surface along slip bands.[17]

It is well known that $\Sigma 3$ coherent TBs in face-centered cubic (f.f.c) material, which correspond to [111] slip planes, are preferential sites for fatigue crack initiation,[18–23] especially at low strain amplitudes. Due to the elastic anisotropy, high stress concentration near TBs may develop[2,21,23–26] and results in intense slip band activity along or in the vicinity of TBs.

In Ni-based superalloys, TBs have also been reported as preferential sites for fatigue crack initiation in LCF, HCF, and VHCF at room and intermediate temperatures.[2–5,27]

On the one hand, cracks were found to appear along or very near to TBs in relation with highly localized slip bands parallel to the TBs plane.[6,7,28] In these cases, high values of the Schmid factor on the slip system parallel to the TB, of the difference of the Young's modulus along the loading direction axis on each side of the TB, and of the TB length at surface were identified as favoring local crystallographic condition for fatigue crack formation along TBs.[4,5,29]

On the other hand, impingement of slip bands arrested at the TB may also lead to a crack,[3] owing to the high energy of TBs against slip transmission which may result in the formation of dislocation pile-ups and associated stress concentration. Such a cracking mode has been shown experimentally based on TEM observations[29] and DIC–EBSD measurements.[10] This has also been supported by molecular dynamics simulations.[30]

Moreover, in some cases, cracks have been found to initiate due to the interaction of slip bands along a TB with a general grain boundary which results in the development of significant local crystallographic rotation (up to ~ 10 deg) within a small region in the neighboring grain, referred to a micro-volume.[31]

To sum up, though it is well established that fatigue crack initiation in polycrystalline Ni-based superalloys occurs preferentially in coarse grain in relation with TBs, there is still a need to identify the different possible cracking modes and the associated local crystallographic configurations. This requires the analysis of numerous crack initiation sites to assess their prevalence for a given fatigue loading conditions.

The aim of the present paper is to study a statistical population of fatigue cracks at TBs for different fatigue conditions. The polycrystalline Ni-based superalloy AD730™ with a bimodal grain structure, including clusters of coarse grains, has been employed as a model material to promote fatigue crack initiation and improve the statistics of analyzed sites, while being sufficiently

representative of cast and wrought γ/γ' Ni-based superalloys used for turbine disks application. Interrupted fatigue tests were carried out using square cross-section specimen with very large flat surfaces for further scanning electron microscopy (SEM) observations and electron backscattered diffraction (EBSD) analyses. After the description of the material and the experimental procedure, the analyses of the different cracking modes and the associated local crystallographic configurations are presented, with emphasis on the role of TBs, as a function at the strain amplitude. Then, the underlying deformation and damage mechanisms are discussed.

II. MATERIAL AND EXPERIMENTAL PROCEDURES

A. Material

The studied material is the polycrystalline Ni-based superalloy AD730™ with the f.c.c γ matrix and the hardening γ' phase ($Ni_3(Al, Ti)$ structure $L1_2$). The chemical composition, reported from References 32, is detailed in Table I.

The grain structure is obtained by specific forming steps followed by a heat treatment (4 hours at 1080 °C/air quench) and an aging treatment (8 hours at 730 °C). An image of the microstructure obtained by EBSD and the resulting distribution are presented in Figure 1 (grain size is defined as the equivalent diameter of 2D reconstructed grains in which TBs have been excluded). The grain size is fine on average (15 μm) with a bimodal distribution. Coarse grains are observed in bands/clusters homogeneously distributed in fine grains. Most of the coarse grains have an equivalent diameter lower than 50 μm (20 μm on average) with the presence of few very coarse grains with diameters, ranging from 50 and 100 μm.

As shown in Figure 1, the studied material does not exhibit any overall crystallographic texture and possesses a large population of $\Sigma 3$ coherent twin boundaries (about one-third of the total boundary length).

The aforementioned heat treatment sequence was applied to all the bar from which the fatigue specimens were machined in order to control the intragranular precipitation structure. The γ' precipitates were characterized with a SEM-FEG (JEOL 7000) in the heads of the specimens after manual/electrolytic polishing and chemical etching [33 pct HNO_3 and 66 pct HCl (vol. parts)], which dissolved the γ' phase. Figure 2 shows the three types of precipitates characterized and classically observed in gamma/gamma' superalloys for subsolvus heat treatment. The intragranular precipitation

Table I. Chemical Composition of AD730™

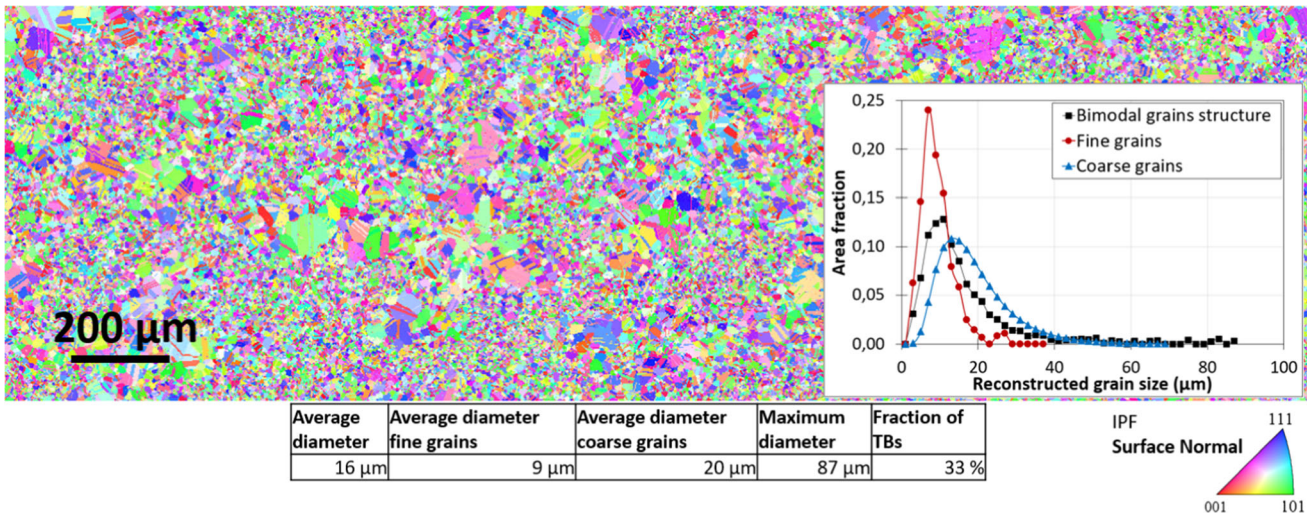| Ni	Fe	Cr	Co	Mo	W	Al	Ti	Nb	B	C	Zr
Base	4.0	15.7	8.5	3.1	2.7	2.25	3.4	1.1	0.01	0.015	0.03

Fig. 1—Representative bimodal grains structure obtained by EBSD and corresponding area-weighted grain size distributions and averages provided for all grains as well as for fine and coarse grains separately.
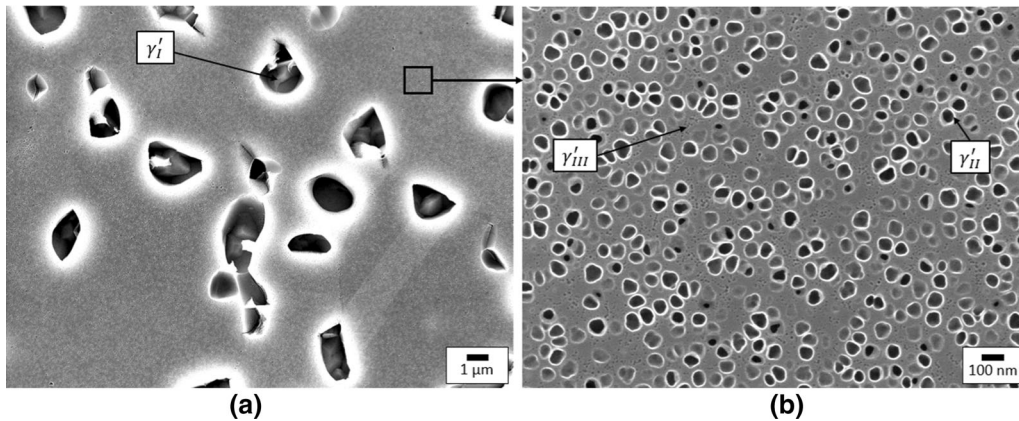
Average diameter	Average diameter fine grains	Average diameter coarse grains	Maximum diameter	Fraction of TBs
16 μm	9 μm	20 μm	87 μm	33 %

(a) **(b)**

Fig. 2—Precipitation structure. (a) Primary precipitates γ'_I. (b) Secondary γ'_{II} and tertiary γ'_{III} intragranular precipitates.

observed is comparable for all specimens with secondary γ'_{II} precipitates diameter of about 50 nm (obtained using the image analysis procedure described in Reference 33).

Few non-metallic inclusions (titanium nitrides TiN surrounded by a titanium and niobium carbide (Ti, Nb) C shell) of about 10 μm are also present in the AD730™.[34]

B. Mechanical Tests and Analysis of Cracking Sites

Uniaxial tension–compression fatigue tests were performed at room temperature, in air, using an Instron 8862 type electromechanical machine. Tests were carried out in strain control mode, with a load ratio of $R_\varepsilon = -1$, a triangular signal, and a frequency of 0.5 Hz. Fatigue tests were performed using 6 × 6 mm² square cross-section specimens, exhibiting very large flat 6 × 12 mm² rectangular surfaces for further observations, with two strain amplitudes (± 0.27 and ± 0.52 pct). At low strain amplitude (± 0.27 pct), the test was interrupted at ~ 20, ~ 30 and ~ 60 pct of the fatigue life.

At high strain amplitude (± 0.52 pct), the test was interrupted at ~ 5 pct of the fatigue life.

The selected strain amplitudes and corresponding interruption sequences were defined based on several preliminary fatigue tests carried out using conventional cylindrical specimens (having a 4.37 mm and a 13 mm gauge diameter and length, respectively), including several preliminary interruptions for intermediate observations, in order to determine the total fatigue life as well as the number of the cycles resulting in a sufficient number of early cracks for a given loading condition.

After each interruption, SEM mappings of the faces of square cross-section specimens were performed to detect crack initiation sites. Subsequent analyses were based on EBSD and higher magnification SEM-FEG images.

It should be noted that, after mechanical polishing of each specimen up to a 1 μm diamond spray finish, the faces of square cross-section specimens were also electropolished at 4 °C under 45 V using a solution made of 10 pct (vol pct) perchloric acid in methanol.
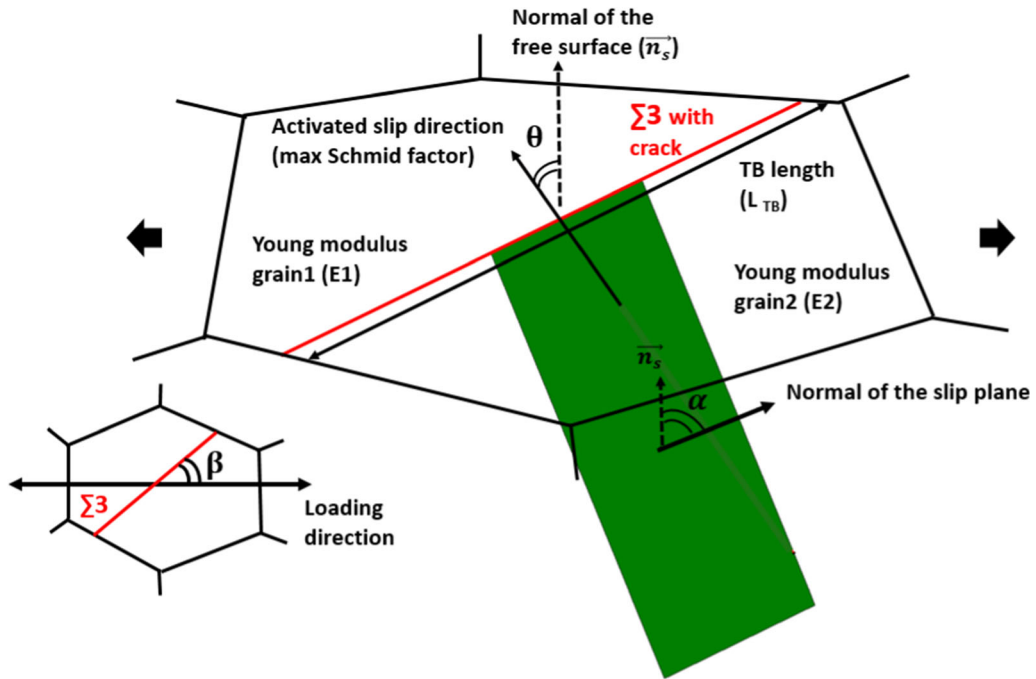
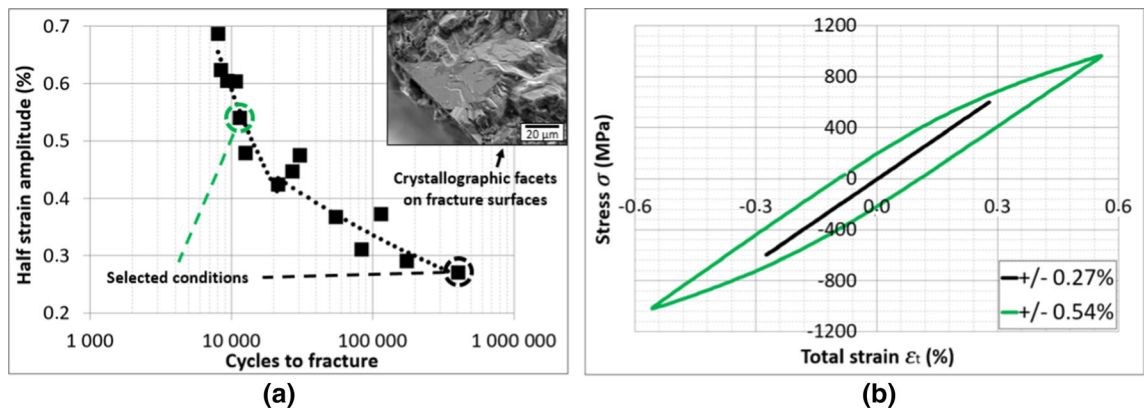Fig. 3—Schematic of the parameters analyzed for a crack along a TB.

(a)   **(b)**

Fig. 4—(*a*) S–N curve with an example of crystallographic facet observed on a fracture surface for $\pm$ 0.3 pct. (*b*) Hysteresis loops at mid-life for the two selected conditions ($\pm$ 0.3 and $\pm$ 0.54 pct).

For each cracked coherent TB, EBSD data were used to compute (Figure 3):

- The TB's length (L_{TB}).
- The maximum Schmid factor (μ) of slip systems composed of {111} slip plane parallel to the TB.
- The difference between the elastic modulus along the loading axis ($\Delta E = |E1 - E2|$) of the two grains at each side of the TB.
- The angle (β) between the trace of the crack (pr TB) at surface and the loading axis (used to identify the {111} slip plan parallel to the TB).
- The angle (θ) between the activated slip direction and the normal to the free surface.
- The angle (α) between the normal of the activated slip plan (or TB plan) and the normal to the free surface.

The elastic modulus difference ΔE was computed using values of the three independent elastic constants of cubic material reported for the AM1 superalloy.[35]

III. RESULTS

A. *Fatigue Life and Fracture Surface*

Fatigue life results, obtained from preliminary tests on conventional cylindrical specimens, are shown in Figure 4(a) in which two distinct domains can be seen. At high applied strain amplitudes ($> \pm$ 0.4 pct), the fatigue loops a macroscopically opened, while at lower applied strain amplitudes ($< \pm$ 0.4 pct) the macroscopic behavior remains linearly elastic, as shown by the stress–strain curves at mid-life reported in Figure 4(b).

This fatigue behavior has also been observed for interrupted tests on square cross-section specimens.

Based on the preliminary results, the following parts of this article concentrate on crack initiation sites detected at surface of square cross-section specimens for interrupted fatigue tests for the 2 selected conditions, *i.e.*, low strain amplitude ($\pm$ 0.27 pct) and high strain amplitude ($\pm$ 0.52 pct).

B. Types of Crack Initiation Sites

For both loading conditions, almost all the cracks initiate at clusters of coarse grains. For the specimens subjected to low strain amplitude ($\pm$ 0.27 pct), SEM mappings were performed on 3 faces (corresponding to ~ a 150 mm^2 analyzed surface) in which 86 cracks were detected at 60 pct of the fatigue life. This corresponds to a low crack density of 0.77 cracks/mm^2. Only 6 additional new cracks were detected between 20 and 60 pct of the fatigue life. At low strain amplitude, very few slip markings are observed only in the vicinity of the cracks. Conversely, slip bands and cracks are much more numerous at high strain amplitude. Thus, it was chosen to detect all the cracks in an area of 2000 × 700 μm^2, as well as a few other sites interesting outside of this area. 56 cracks were identified, corresponding to a density of 39 cracks/mm^2. This density is probably underestimated due to the high density of slip bands and the difficulty, at some point, to differentiate a slip band from a crack with the chosen SEM-FEG magnification.

Examples of identified crack initiation sites are shown in Figures 5 and 6 at low and high strain amplitudes, respectively, while their statistics of occurrence are reported in Figure 7. It should be noted that, in Figures 5 and 6, coherent Σ3 TBs are shown in red while all other boundaries, referred to as general grain boundaries, are shown in black (grains were formerly defined based on a 2 deg misorientation tolerance angle).

At low strain amplitude ($\pm$ 0.27 pct), except for a few cracks (~ 5 pct) which are too long to clearly identify the initiation sites, all detected cracks appear in relation with TBs (Figure 7). In most cases (~ 80 pct), crack is observed along a single TB (Figure 5(a)).

In other cases (~ 20 pct), cracks are observed along two continuous TBs which form a multiple junction (Figure 5(b)). The junction is systematically composed of several TBs (linked by a short segment of a general grain boundary) and sometimes some grain boundaries.
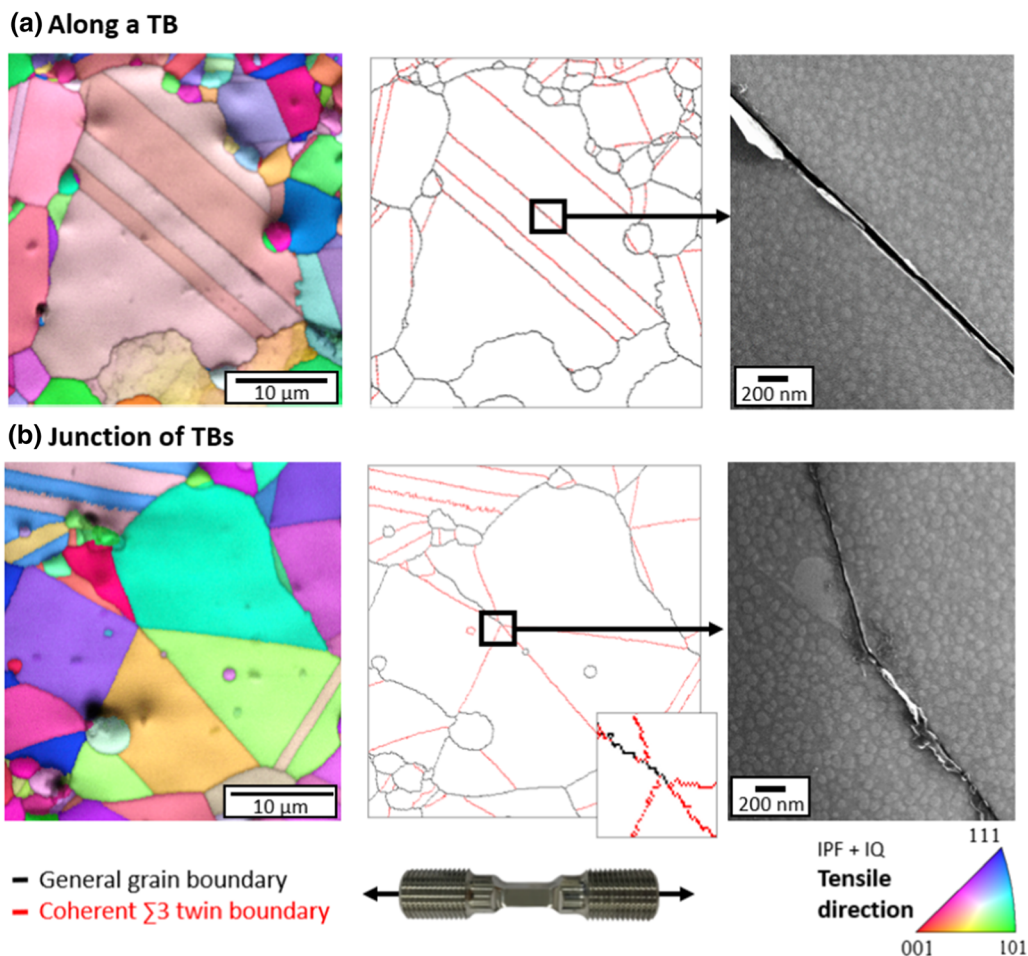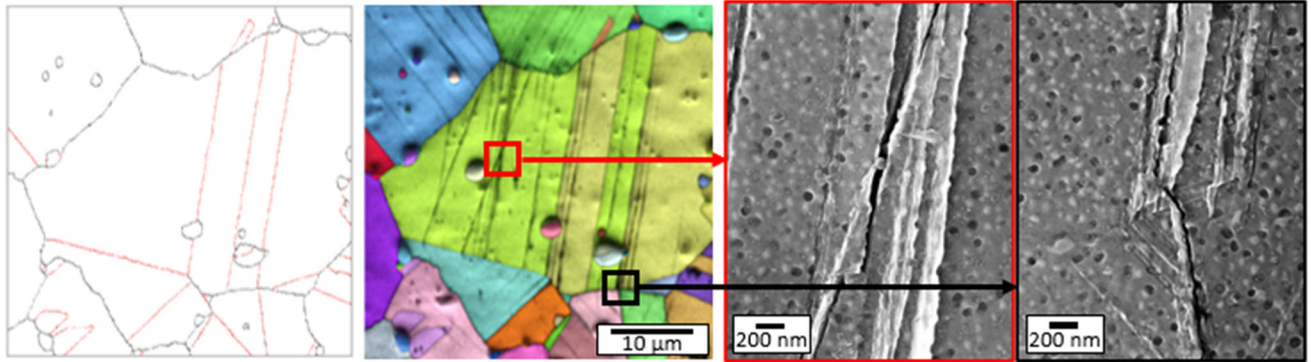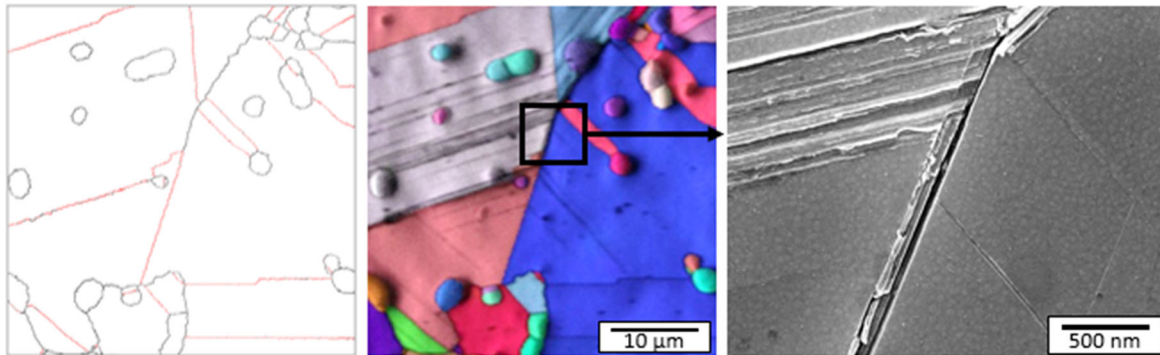

Fig. 5—Typical of crack initiation sites at ± 0.27 pct, the red boundaries are TBs and the black boundaries are general grain boundaries. (*a*) Crack at a TBs junction. (*b*) Crack along a TB (Color figure online).
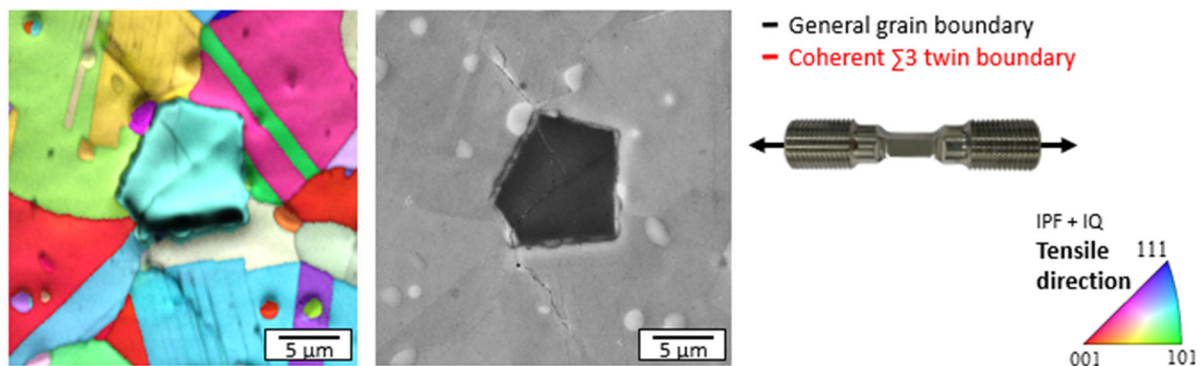
Fig. 6—Type of crack initiation sites at ± 0.52 pct. (*a*) Crack along a TB and transgranular crack. (*b*) Crack at a general grain boundary. (*c*) Crack on a particle (Color figure online).

Figure 8 shows additional examples of cracks along TBs for the 2 strain amplitudes.

At low strain amplitude, slip markings are not pronounced and corresponds mostly to rather small extrusions, as shown in Figures 5 and 8(a), along the crack which seems to coincide with the TB. As shown in the inset in Figure 8(a), short slip markings are also observed within micro-volumes which develop at the intersection between the slip bands along the TB and the adjacent grain boundary. Such micro-volumes, detected by local crystallographic rotation up to 8 deg, were observed for 20 pct of the cracks along TBs at low strain amplitude.

At high strain amplitude, the formation of the crack occurs along one slip band or among several parallel slip bands. In some cases, as in Figure 8(b), it can be identified that the crack developed along slip band parallel and right next to the TB. However, in most cases, it is difficult to determine whether the crack coincides with the TB or not.

It should be noted that the interesting configurations of cracks at multiple TBs junctions, observed only at low stain amplitude for 20 pct of the initiation sites, have not been included in the following, since it requires specific analyses and descriptors, probably almost on a case-by-case basis. This configuration, not mentioned in the literature to the authors' very best knowledge, could

be specific to the process history of the bimodal microstructure studied. This will be studied in a forthcoming article.

C. Analyses of Crack Initiation Sites Along TBs

In order to discuss the local crystallographic configurations which promote crack initiation along TBs, statistics about the different quantities introduced in Figure 3 were performed. Average value and standard deviation are reported in Table II, while frequency distributions and scatter plots are shown in Figures 9 and 10, respectively.

First, as shown in Table II, at both strain amplitudes, the average length of TBs that develop cracks is only slightly larger than 20 μm, i.e., the average grain size within the coarse grain region of the bimodal microstructure, in which cracks were observed in almost all cases. The differences of Young's modulus are also very comparable for both strain amplitudes.

Then, regarding the maximum Schmid factor, as shown in Table II and Figure 9(d), a broader distribution is noticed at high strain amplitude (ranging mostly from 0.4 to 0.5), while at low strain amplitude Schmid factors are larger than 0.48 for about two-third of the cracked TBs.

The most significant difference between the two loading conditions is related to the ranges taken by the three studied angles (Figures 9(a) through (c)), in particular the angle θ between the slip direction and the normal to the free surface. Indeed, as shown in Figure 9(a), the angle θ is larger than 60 deg for all studied configurations at low strain amplitude. Conversely, at high strain amplitude, the θ angle ranges from 30 to 60 deg for most of the cases, with higher values for a few initiation sites. As already noted for the Schmid factor, the scatter is more important at high strain amplitude.

The data are also reported using scatter plots in Figures 10 and 11. In particular, scatter plots of the 3 studied angles are reported Figures 11(a) and (b) with Schmid factor contour background, to gather synthetically the different information and highlight the relatively well-distinct domains occupied by the crack population of each loading condition. It should be emphasized that, in Figures 11(a) and (b), there is a non-existence domain of some angle pairs. For instance, if the slip plane is parallel to the free surface (i.e., $\alpha = 0$ deg), the slip direction is also necessarily parallel to the free surface ($\theta = 90$ deg). Moreover, each possible pair of angles corresponds to a range of crystallographic orientations and thus a range of maximal Schmid factor. In the Schmid factor background in Figures 11(a) and (b), only the maximal value obtained for each pair is reported, referred to as potential maximum Schmid factor. This corresponds to the projection of the upper surfaces of the 3D scatter plots (Figures 11(c) and (d))
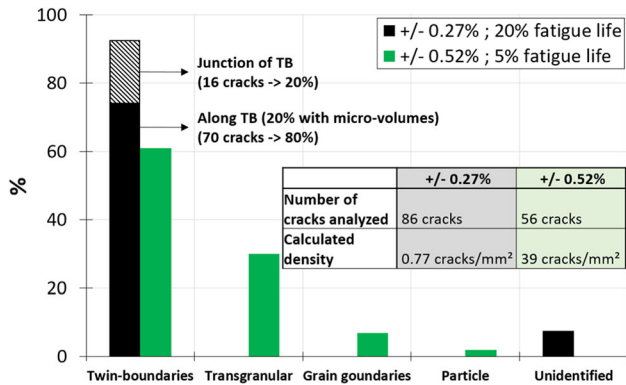

Fig. 7—Proportions of the initiation sites and cracks density for ± 0.27 and ± 0.52 pct.
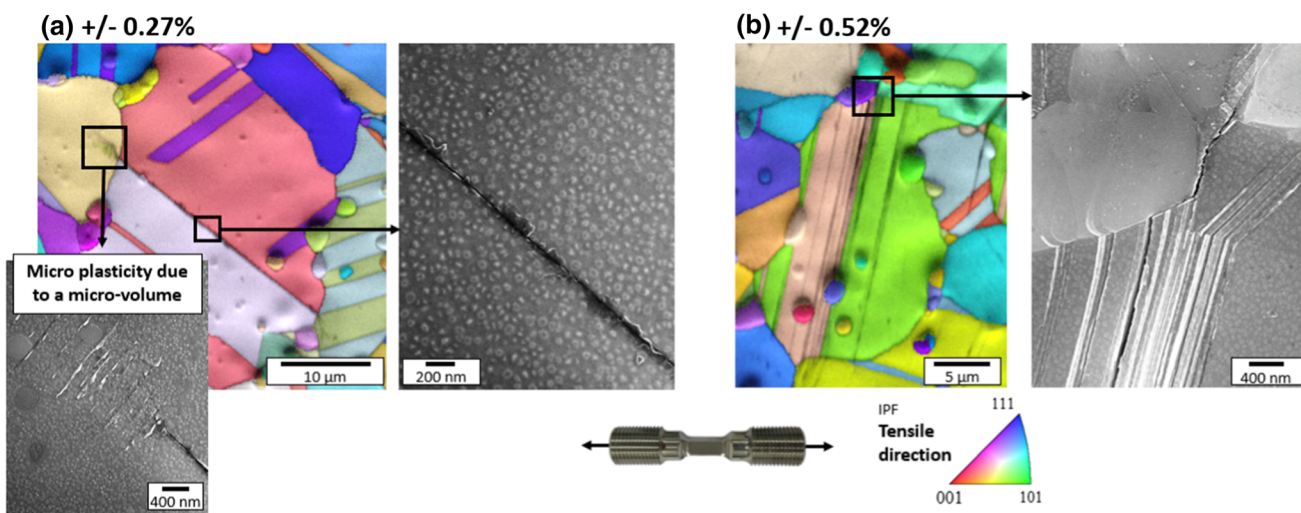

Fig. 8—Examples of cracks along TBs (EBSD and SEM-FEG observations) at (a) low strain amplitude (one inset shows slip markings within a micro-volume) and at (b) high strain amplitude.

Table II. Average Values and Standard Deviations of the Quantities Systematically Calculated for All Cracks Along the TBs for ± 0.27 and ± 0.52 Pct

|	TB Length (L_{TB})/Slip Band Length		Young Modulus Difference (ΔE)		Schmid Factor		Angle Activated Slip Direction/ Normal Surface (θ)		Angle Surface Crack Trace/ Loading Direction (β)		Angle Normal Activated Slip Plane/Normal Surface (α)	
	Average (μm)	SD (μm)	Average (GPa)	SD (GPa)	Average	SD	Average (deg)	SD (deg)	Average (deg)	SD (deg)	Average (deg)	SD (deg)
± 0.27 Pct Along TBs	23.4	10.2	46.3	30.1	0.481	0.015	78.0	9.7	47.2	6.8	74.3	9.4
± 0.52 Pct Along TBs	22.2	10.1	42.3	34.5	0.448	0.042	46.6	6.8	68.2	13.5	60.8	9.2
± 0.52 Pct Transgranular	20.7	12.4			0.467	0.028	48.7	14.5	71.3	11.9	56.5	7.2
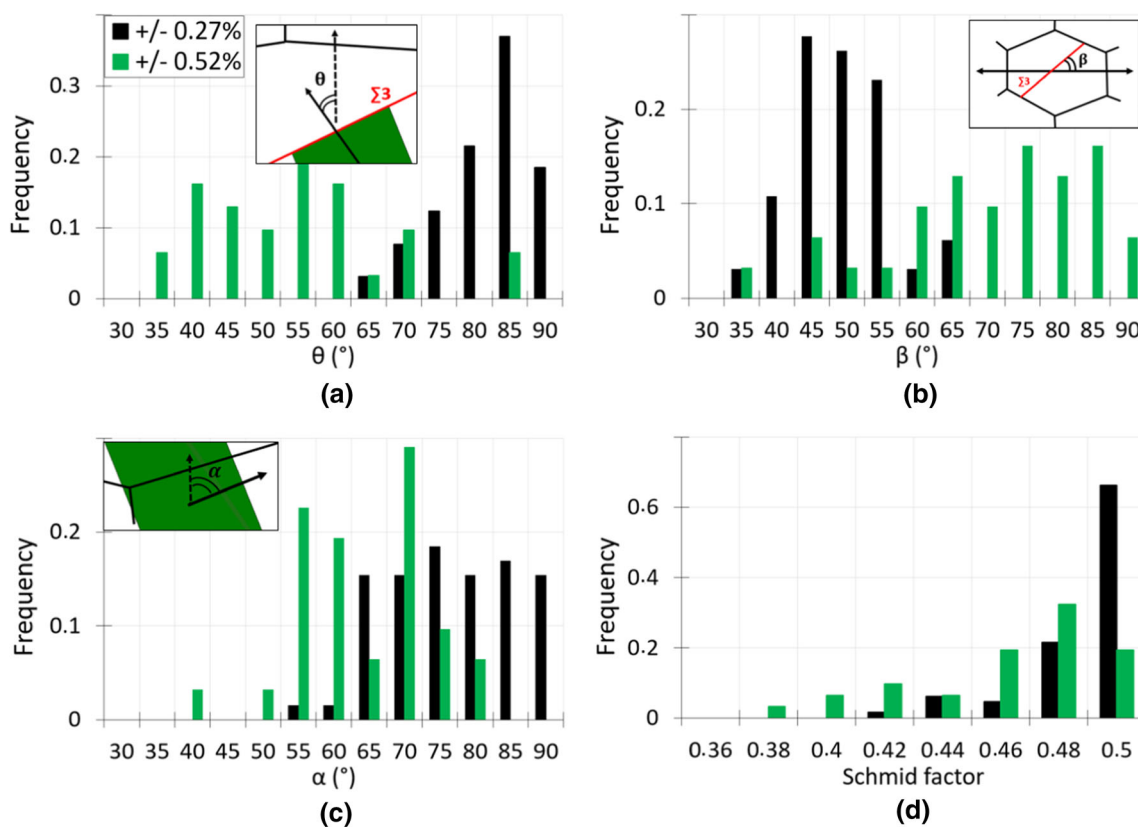
Fig. 9—Frequency histograms for both strain amplitudes (a) angle θ between the activated slip direction and the normal to the free surface, (b) angle β between the trace of the crack at surface and the loading direction, (c) angle α between the normal to the activated slip plane and the normal to the free surface, (d) maximum Schmid factor on the slip plane parallel to the TB plane.

(obtained based on 40,000 randomly drawn crystallographic orientations).

IV. DISCUSSION

A statistical population of microcracks was detected and analyzed, at early stage of their formation, on the surface of γ/γ' Ni-based superalloy AD730™ with bimodal grain structure, fatigued at room temperature and at two different strain amplitudes. The low strain amplitude condition, within the macroscopically linear elastic regime (with applied stress of about 55 pct of the 0.02 pct offset yield stress), results in a very low crack density (< 1 crack/mm^2) with only few signs of localized slip bands activity observed. The high strain amplitude condition is slightly above the elastic limit (corresponding to about 0.14 pct plastic strain amplitude at mid-life)
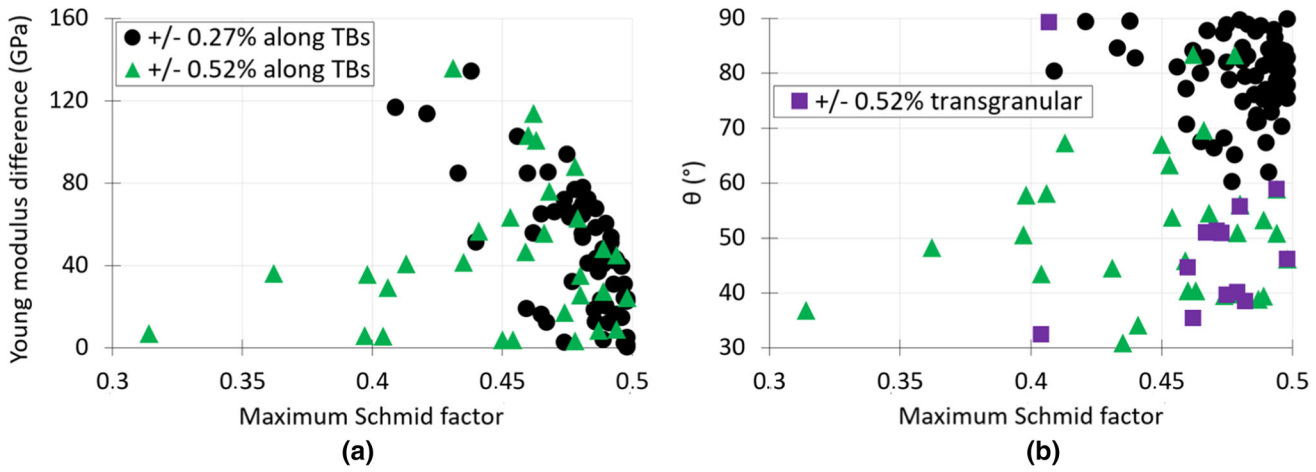
Fig. 10—(a) Young's modulus difference between the parent grain and the twin and (b) angle θ between the activated slip direction and the normal to the free surface as a function of the maximum Schmid factor on the slip plane parallel to the TB plane for each crack initiation site along a TB and transgranular for the two loading condition.
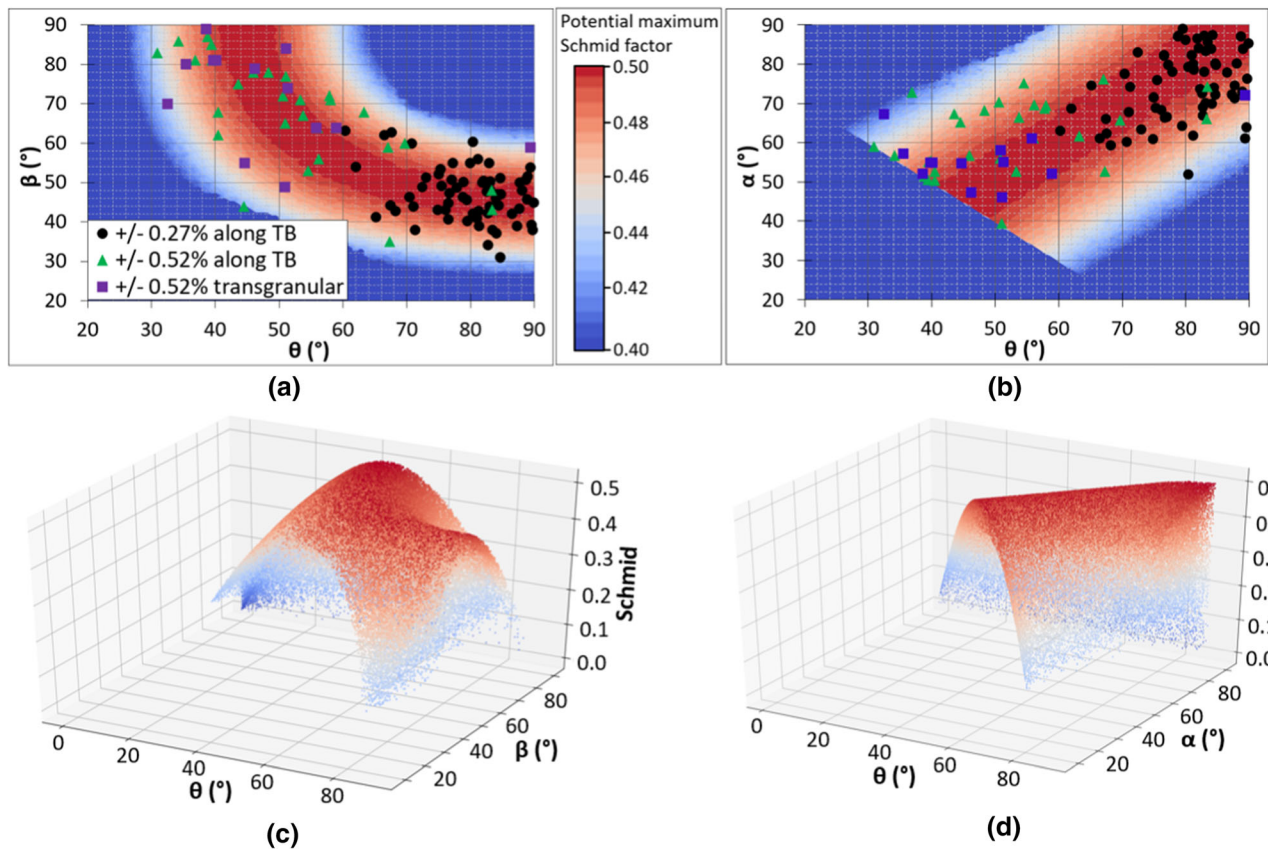

Fig. 11—(a) Pair of angles (θ, β) and (b) pair of angles (θ, α) for each crack initiation site along a TB and transgranular with colored background representing the maximum potential Schmid factor. (c, d) Corresponding 3D graphs where each point corresponds to a slip direction activated on the 4 octahedral planes for 40,000 randomly orientations (Color figure online).

and results in an intense plastic slip band activity and higher crack density (~ 50 cracks/mm²) from 5 pct of the fatigue life. In both loading conditions, cracks are initiated within clusters of coarse grains of the studied bimodal microstructure and mostly along TBs.

The analyses of classical geometric/crystallographic parameters (Schmid factor, Young's modulus difference, TB length, orientation of slip system with respect to free surface and loading direction) enable the identification of some preferential conditions which promote crack initiation which are consistent with other studies of the

literature. In particular, the results related to the Schmid factor and the difference of Young's modulus (Figure 10(a)), as well as those related to the inclination of the slip direction with respect to the surface, *i.e.,* angle θ, show comparable trends with those reported by Stinville *et al.*[5] in René88DT superalloy in the LCF and VHCF regimes. However, the importance of the Young's modulus difference is less pronounced, especially in the high strain amplitude regime, than the one reported in Reference 5. The effect of TB length also seems to be less important than the one noticed in Reference 5. This could probably arise from the specific bimodal grain structure considered in the present study.

However, in general, it cannot be expected that the different considered parameters enable the definition of a strict and single criterion to predict fatigue crack initiation sites (see *e.g.,* References 36 and 37 in the case of transgranular fatigue crack initiation in austenitic steels). Indeed, the actual local stress/strain fields and slip bands activity within a grain depend on its own orientation, size, and 3D morphology but also on those of all neighboring grains, as it can be assessed using crystal elasto-plasticity type full-field simulations.[37–40] Local stresses within a polycrystal may differ from the macroscopically uniaxial applied loading in a more important and complex manner in the presence of TBs, which requires to take into account the full 3D grains and twins structures in the vicinity of the considered TB. Schmid factors of the slip plane parallel to the TB and the difference of Young's modulus across the TB are too indirect indicators of the possible enhancement of resolved shear stress and plastic slip activity near TB.

As presented in Section III–C, one of the most noteworthy results of this study is the identification of relatively well-delimited domains, at each strain amplitude, for the orientation of the TBs along which crack initiation was observed. According to the data reported in Table II, as well as in Figures 9, 10, and 11, a schematic of the two typical configuration is proposed in Figure 12.

At low strain amplitude (Figure 12(a)), the TB plane tends to be normal to the free surface (*i.e.*, angle α close to 90 deg) and to be well oriented for slip with respect to the loading axis (*i.e.*, angle β close to 45 deg). Moreover, the slip direction which is assumed to be activated is almost parallel to the free surface (*i.e.*, angle θ close to 90 deg), and thus also inclined at about 45 deg with respect to the loading axis (*i.e.,* Schmid factor close to 0.5). This type of configuration is very close to the ideal one referred to as a well-oriented facet of type A by Sauzay and Jourdan[38]. To a lesser extent, the typical configurations observed at high strain amplitude (Figure 12(b)) are close to a well-oriented facet of type B, for which slip plane normal and slip direction are inclined at 45 deg with respect to the tensile axis and to the free surface.

Accordingly, this latter type of slip configuration parallel to the TB should enable the formation of a significant surface relief resulting from slip bands intrusions and extrusions.[41] Extrusions height were reported in several studies on pure metals as a possible criterion for micro-cracks formation in both single crystal and polycrystals in a transgranular mode.[12–14,16,42] Thus, it is likely that the formation of cracks along a TB at high strain amplitude is governed by the height of extrusion resulting from a slip band parallel and adjacent to the TB. This hypothesis is supported by the fact that the angles relative to the slip system configurations (θ, β, α) of the transgranular cracks are in the same ranges as for the cracks along the TBs (see Table II, Figures 10(b) and 11(a) and (b)).
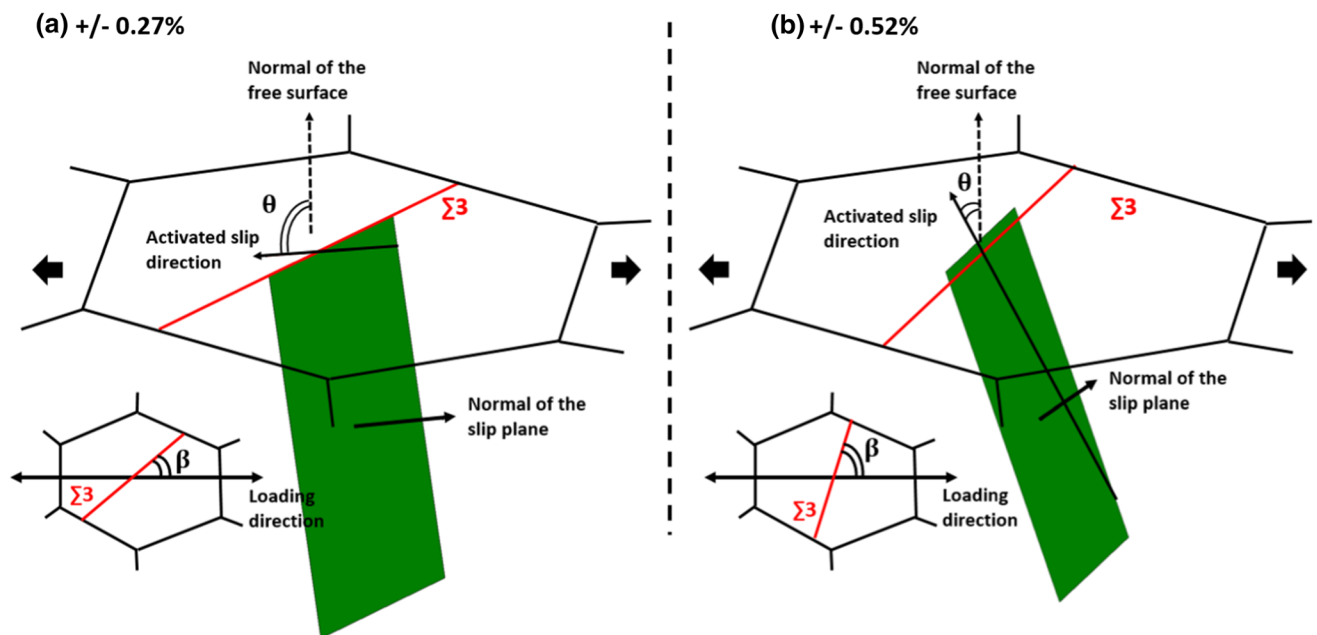

Fig. 12—Schematics of typical TB cracking configurations at (*a*) low strain amplitude and (*b*) high strain amplitude.

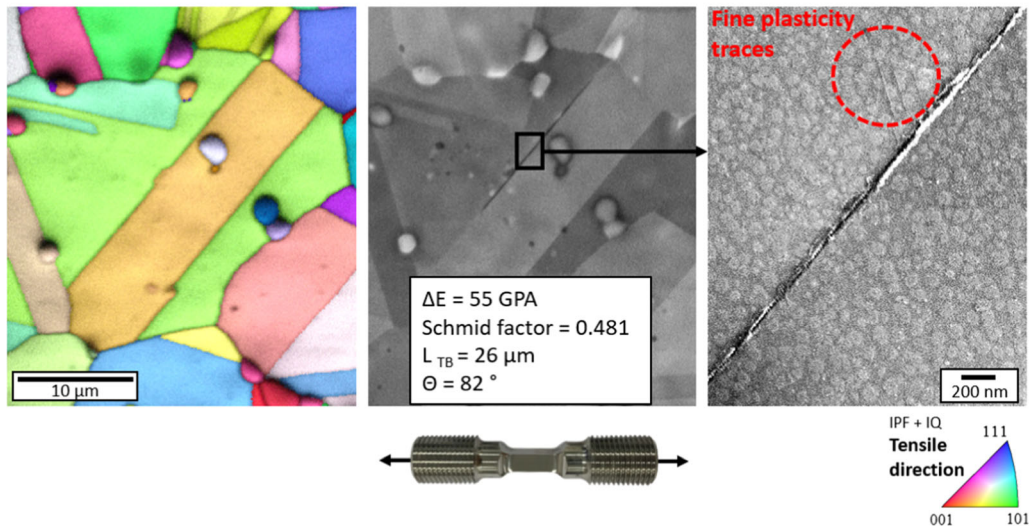+/- 0.27% : Example of crack initiation in the center of the grains

ΔE = 55 GPA
Schmid factor = 0.481
L_{TB} = 26 μm
Θ = 82 °

Fine plasticity traces

IPF + IQ
Tensile direction

10 μm

200 nm

Fig. 13—Example of crack initiations along TBs in the center of the grains.

ΔE = 43 GPA / L_{TB} = 14 μm / Θ = 86 ° / Schmid factor = 0.493

Schmid = 0.429
Schmid = 0.494
Schmid = 0.306

200 nm

(a)

ΔE = 22 GPA / L_{TB} = 32 μm / Θ = 78 ° / Schmid factor = 0.498

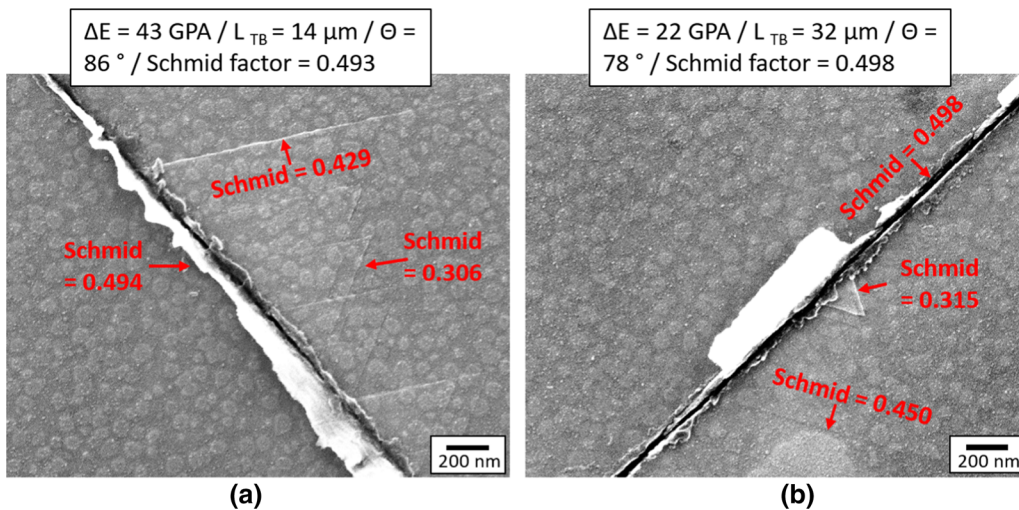Schmid = 0.498
Schmid = 0.315
Schmid = 0.450

200 nm

(b)

Fig. 14—(a, b) SEM-FEG observations of slip traces near TBs cracks at low strain amplitude (0.27 pct) in the center of the grain.

Conversely, at low strain amplitude, the identified configurations should not be prone to create a pronounced surface topography (due to angle θ close to 90 deg). Stinville et al.[5] have taken this angle into account in their fatigue crack initiation criterion by explaining that a slip direction parallel to the free surface does not release dislocations and therefore accumulates plastic deformation. Jiang et al.,[43] based on SEM-DIC strain measurements, have correlated these configurations of slip with low incidence to very high in-plane shear strains. Then, it can be inferred that the interaction between a slip band parallel to the TB and the adjacent grain boundary could play a role in the micro-crack formation process. In the case of difficult slip transmission, this may result in the formation of a micro-volume, as shown in Figure 8(a), from which damage may

initiate.[31,44] Additional analyses based on slip transmission criteria[30,31,44] also support this assumption.

However, such configurations with microvolumes were observed for only 20 pct of the studied initiation sites in the present study. For the remainder part, some configuration clearly indicates that the crack has initiated at the center of the TB, as shown in the example (whose characteristics are in the average) reported in Figure 13. It should be noted that cracks with and without micro-volumes have comparable incidences of slip directions with respect to the free surface (angle θ). Another crack initiation process should operate in such a case.

At low strain amplitude, very thin extrusions can be observed along the TB cracks, as shown in Figures 5(a) and in 8(a). Additional interesting examples are provided in Figure 14. The formation of a significant

surface relief despite very low incidence ($\theta > 80$ deg) is somewhat surprising. It should be reminded that the angle θ is computed for the slip direction with the highest Schmid factor (very close to 0.5 for the two considered examples) among the three possible slip directions within the considered slip plane. However, this observation could result from (1) a very intense slip in the considered slip direction and/or (2) the activation of another slip direction within the slip plane parallel to the TB. These two possible explanations should require that the local stress states significantly differ from the macroscopic uniaxial loading. The variability of observed extrusions height as well as the presence of slight slip markings associated with low Schmid factors support the presence of particularly intense stress concentrations for these configurations.

It is interesting to point out that the crack initiation sites along TBs observed in this bimodal microstructure exhibit very similar characteristics than those reported in the previous studies for more conventional microstructures with a homogeneous grain size (see beginning of the discussion). This suggests that the presence of small grains around coarse grain clusters in which cracks nucleate may not modify significantly the crack formation mechanisms. However, a possible effect on the crack initiation kinetics may result from heterogeneities of stress and strain state within fine grain matrix or coarse grain clusters. Moreover, the occurrence of crack initiation at multiple junctions of TBs at low strain amplitude is possibly related to this bimodal microstructure.

A better understanding of the effective operating deformation and damage modes requires additional investigations based on the following:

- High-resolution SEM-FEG and/or TEM observations, especially in appropriate cross-section of slip bands and crack using FIB.[7,45]
- High-resolution measurements of local strain using DIC-based techniques.[7,25–27,43,46]
- 3D grain structure reconstruction[37,47] and corresponding full-field crystal elasto-plasticity simulations of local stress state and slip activity.

These types of investigation based on advanced techniques can be carried out using a limited number of configurations of crack initiation sites selected as representative cases owing to the obtained statistics.

V. CONCLUSIONS

Early stages of fatigue crack formation in the polycrystalline Ni-based superalloy AD730™ with a bimodal grain size distribution were studied at room temperature and at two strain amplitudes in each of the two domains highlighted in the fatigue life curve. The nature of initiation sites was studied for a statistical population of cracks, which were found to initiate within clusters of coarse grains. For the two considered loading conditions, the formation of cracks takes place predominantly along relatively long TBs. However, a non-negligible

amount of transgranular cracks initiated along slip bands were observed at high strain amplitude, while several cracks initiated at multiple TBs junctions were detected at low strain amplitude. The orientations of the slip systems associated with cracks along TBs are the major characteristics that differs between the two loading conditions, which possibly suggests two different operating crack initiation mechanisms.

At high strain amplitude, the characteristics of the cracks along the TBs are close to transgranular cracks. In both cases, the orientations of the activated slip directions are prone to create significant surface relief, leading in most cases to the formation of microcracks that takes place along slip bands parallel to the TB for a critical extrusion height.

On the contrary, at small strain amplitude, the slip directions of primary slip system are almost parallel to the free surface. This suggests that initiation is related to accumulation of plastic strain and interactions between slip bands and grain boundaries, without creation of significant surface relief. This is supported by the observation of micro-volumes at the intersection of some cracks along a TB and the adjacent grain boundary. However, some cracks also initiate in the center of the TBs, accompanied very thin extrusions related to slip parallel to TBs as well as short slip markings non-parallel to TBs, which indicate concentrations of local mechanical stresses probably due to complex 3D grain parent—twin configurations.

CONFLICT OF INTEREST

The authors declare that they have no conflict of interest with the work presented in this article.

REFERENCES

1. R.C. Reed: *The Superalloys, Fundamental and Applications*, Cambridge University Press, Cambridge, 2008.

2. J. Miao, T.M. Pollock, and J. Wayne Jones: *Acta Mater.*, 2009, vol. 57(20), pp. 5964–74.
3. M.D. Sangid, H.J. Maier, and H. Sehitoglu: *J. Mech. Phys. Solids*, 2011, vol. 59(3), pp. 595–609.
4. C.A. Stein, A. Cerrone, T. Ozturk, S. Lee, P. Kenesei, H. Tucker, R. Pokharel, J. Lind, C. Hefferan, R.M. Suter, A.R. Ingraffea, and A.D. Rollett: *Curr. Opin. Solid State Mater. Sci.*, 2014, vol. 18(4), pp. 244–52.
5. J.C. Stinville, W.C. Lenthe, J. Miao, and T.M. Pollock: *Acta Mater.*, 2016, vol. 103, pp. 461–73.
6. B.A. Lerch, N. Jayaraman, and S.D. Antolovich: *Mater. Sci. Eng.*, 1984, vol. 66(2), pp. 151–66.
7. J.C. Stinville, E. Martin, M. Karadge, S. Ismonov, M. Soare, T. Hanlon, S. Sundaram, M.P. Echlin, P.G. Callahan, W.C. Lenthe, V.M. Miller, J. Miao, A.E. Wessman, R. Finlay, A. Loghin, J. Marte, and T.M. Pollock: *Acta Mater.*, 2018, vol. 152, pp. 16–33.
8. C.W. Brown, J.E. King, and M.A. Hicks: *Met. Sci.*, 1984, vol. 18(7), pp. 374–80.
9. D.L. Davidson, R.G. Tryon, M. Oja, R. Matthews, and K.S.R. Chandran: *Metall. Mater. Trans. A*, 2007, vol. 38(13A), pp. 2214–25.
10. J. Rotella and M.D. Sangid: *Fatigue Fract. Eng. Mater. Struct.*, 2020, vol. 43(10), pp. 2270–286.
11. P.J.E. Forsyth: *Nature*, 1953, vol. 171(4343), pp. 172–73.
12. A. Hunsche and P. Neumann: *Acta Metall.*, 1986, vol. 34(2), pp. 207–17.
13. J. Polák: *Mater. Sci. Eng.*, 1987, vol. 92, pp. 71–80.
14. Z.S. Basinski and S.J. Basinski: *Prog. Mater. Sci.*, 1992, vol. 36, pp. 89–148.
15. J.C. Stinville, M.A. Charpagne, A. Cervellon, S. Hemery, F. Wang, P.G. Callahan, V. Valle, and T.M. Pollock: *Science*, 2022, vol. 377(6610), pp. 1065–71.
16. M. Risbet, X. Feaugas, C. Guillemer-Neel, and M. Clavel: *Scripta Mater.*, 2003, vol. 49(6), pp. 533–38.
17. H.S. Ho, M. Risbet, and X. Feaugas: *Acta Mater.*, 2015, vol. 85, pp. 155–67.
18. R.C. Boettner, A.J. McEvily Jr., and Y.C. Liu: *Philos. Mag.*, 1964, vol. 10(103), pp. 95–106.
19. A. Thompson: *Acta Metall.*, 1972, vol. 20(9), pp. 1085–94.
20. T. Sumigawa, T. Kitamura, and K. Ohishi: *Fatigue Fract. Eng. Mater. Struct.*, 2004, vol. 27(6), pp. 495–503.
21. A. Heinz and P. Neumann: *Acta Metall. Mater.*, 1990, vol. 38(10), pp. 1933–40.
22. M. Mineur, P. Villechaise, and J. Mendez: *Mater. Sci. Eng. A*, 2000, vol. 286(2), pp. 257–68.
23. C. Blochwitz and W. Tirschler: *Mater. Sci. Eng. A*, 2003, vol. 339(1–2), pp. 318–27.
24. P. Peralta, L. Llanes, J. Bassani, and C. Laird: *Philos. Mag. A*, 1994, vol. 70(1), pp. 219–32.
25. F. Bourdin, J.C. Stinville, M.P. Echlin, P.G. Callahan, W.C. Lenthe, C.J. Torbet, D. Texier, F. Bridier, J. Cormier, P. Villechaise, T.M. Pollock, and V. Valle: *Acta Mater.*, 2018, vol. 157, pp. 307–25.
26. J.C. Stinville, M.A. Charpagne, F. Bourdin, P.G. Callahan, Z. Chen, M.P. Echlin, D. Texier, J. Cormier, P. Villechaise, T.M. Pollock, and V. Valle: *Mater. Charact.*, 2020, vol. 169, 110600.
27. D. Texier, J. Cormier, P. Villechaise, J.C. Stinville, C.J. Torbet, S. Pierret, and T.M. Pollock: *Mater. Sci. Eng., A*, 2016, vol. 678, pp. 122–36.
28. F.D.L. Cázares, R. Schlütter, T. Jackson, E.I. Galindo-Nava, and C.M.F. Rae: *Acta Mater.*, 2020, vol. 182, pp. 47–59.
29. T.C. Lee, I.M. Robertson, and H.K. Birnbaum: *Metall. Trans. A*, 1990, vol. 21A(9), pp. 2437–47.
30. M.D. Sangid, T. Ezaz, H. Sehitoglu, and I.M. Robertson: *Acta Mater.*, 2011, vol. 59(1), pp. 283–96.
31. B. Larrouy, P. Villechaise, J. Cormier, and O. Berteaux: *Acta Mater.*, 2015, vol. 99, pp. 325–36.
32. A. Devaux, A. Helstroffer, J. Cormier, P. Villechaise, J. Douin, M. Hantcherli, and F. Pettinari-Sturmel: in *8th International Symposium on Superalloy 718 and Derivatives*, Wiley, Hoboken, 2014, pp. 521–35.
33. J.R. Vaunois, J. Cormier, and P. Villechaise: in *Proceedings of the 7th International Symposiumon Superalloy*, TMS, Pittsburgh, vol. 718, 2010.
34. A. Govaere, A.L. Rouffié, J.M. Franchet, D. Galy, C. Dumont, A. Devaux, C. Crozet, P. Kontis, P. Villechaise, and J. Cormier: in *Superalloys 2020*, Springer, Cham, 2020, pp. 591–602.
35. A. Gaubert, M. Jouiad, J. Cormier, Y. Le Bouar, and J. Ghighi: *Acta Mater.*, 2015, vol. 84, pp. 237–55.
36. P. Mu, V. Aubin, I. Alvarez-Armas, and A. Armas: *Mater. Sci. Eng. A*, 2013, vol. 573, pp. 45–53.
37. L. Signor, P. Villechaise, T. Ghidossi, E. Lacoste, M. Gueguen, and S. Courtin: *Mater. Sci. Eng. A*, 2016, vol. 649, pp. 239–49.
38. M. Sauzay and T. Jourdan: *Int. J. Fract.*, 2006, vol. 141(3), pp. 431–46.
39. A. Zeghadi, S. Forest, A.F. Gourgues, and O. Bouaziz: *Philos. Mag.*, 2007, vol. 87(8–9), pp. 1425–46.
40. R. Brenner, R.A. Lebensohn, and O. Castelnau: *Int. J. Solids Struct.*, 2009, vol. 46(16), pp. 3018–26.
41. J. Man, K. Obrtlik, C.H. Blochwitz, and J. Polak: *Acta Mater.*, 2002, vol. 50(15), pp. 3767–80.
42. J. Polák, J. Man, and K. Obrtlík: *Int. J. Fatigue*, 2003, vol. 25(9–11), pp. 1027–36.
43. R. Jiang, F. Pierron, S. Octaviani, and P.A.S. Reed: *Mater. Sci. Eng. A*, 2017, vol. 699, pp. 128–44.
44. J. Genée, L. Signor, and P. Villechaise: *Mater. Sci. Eng. A*, 2017, vol. 701, pp. 24–33.
45. J. Man, T. Vystavěl, A. Weidner, I. Kuběna, M. Petrenec, T. Kruml, and J. Polák: *Int. J. Fatigue*, 2012, vol. 39, pp. 44–53.
46. J.C. Stinville, N. Vanderesse, F. Bridier, P. Bocher, and T.M. Pollock: *Acta Mater.*, 2015, vol. 98, pp. 29–42.
47. M. Jiménez, W. Ludwig, D. Gonzalez, and J.M. Molina-Aldareguia: *Scripta Mater.*, 2019, vol. 162, pp. 261–65.